Lab on a Chip

PAPER

View Article Online
View Journal | View Issue

Cite this: *Lab Chip*, 2019, **19**, 4117

Analyte transport to micro- and nano-plasmonic structures†

N. Scott Lynn Jr., Tomáš Špringer, Jiří Slabý, Barbora Špačková,‡ Michaela Gráfová, Maria Laura Ermini§ and Jiří Homola *

The study of optical affinity biosensors based on plasmonic nanostructures has received significant attention in recent years. The sensing surfaces of these biosensors have complex architectures, often composed of localized regions of high sensitivity (electromagnetic hot spots) dispersed along a dielectric substrate having little to no sensitivity. Under conditions such that the sensitive regions are selectively functionalized and the remaining regions passivated, the rate of analyte capture (and thus the sensing performance) will have a strong dependence on the nanoplasmonic architecture. Outside of a few recent studies, there has been little discussion on how changes to a nanoplasmonic architecture will affect the rate of analyte transport. We recently proposed an analytical model to predict transport to such complex architectures; however, those results were based on numerical simulation and to date, have only been partially verified. In this study we measure the characteristics of analyte transport across a wide range of plasmonic structures, varying both in the composition of their base plasmonic element (microwires, nanodisks, and nanorods) and the packing density of such elements. We functionalized each structure with nucleic acid-based bioreceptors, where for each structure we used analyte/receptor sequences as to maintain a Damköhler number close to unity. This method allows to extract both kinetic (in the form of association and dissociation constants) and analyte transport parameters (in the form of a mass transfer coefficient) from sensorgrams taken from each substrate. We show that, despite having large differences in optical characteristics, measured rates of analyte transport for all plasmonic structures match very well to predictions using our previously proposed model. These results highlight that, along with optical characteristics, analyte transport plays a large role in the overall sensing performance of a nanoplasmonic biosensor.

Received 19th July 2019,
Accepted 12th November 2019

DOI: 10.1039/c9lc00699k

rsc.li/loc

Introduction

In the past decade there has been an extraordinary growth of research into optical affinity biosensors based on plasmonic nanostructures (*i.e.*, nanoplasmonic biosensors).[1–4] In contrast to their surface plasmon resonance (SPR) predecessors based on a continuous metal film,[5] nanoplasmonic substrates are often composed of (metal) plasmonic features dispersed along a dielectric substrate. The architecture of these substrates can take many configurations, ranging from sensors based on positive relief nanodisks,[6] nanorods,[7] nanoprisms,[8] and nanowires,[9] to sensors based on negative relief nanoholes,[10] as well as *N*-particle clusters of both types (*e.g.*, nanorod dimers,[11] nanohole heptamers[12]). Although measurements on these substrates can proceed *via* several modes (*e.g.*, localized surface plasmons, collective resonances, and Fano resonances), they all follow a similar principle when used as a biosensor, whereby the selective capture of analyte by immobilized receptors causes a change in the sensor response.

The orthogonal functionalization of nanoplasmonic substrates – the immobilization of bioreceptors to sensitive regions (*i.e.*, plasmonic hot spots) and passivation of the remaining non-sensitive regions – has been demonstrated to significantly increase biosensing performance when compared to similar substrates with uniform functionalization.[13,14] This performance increase is due to increases in analyte transport: illustrated in Fig. 1 for a SPR and nanoplasmonic biosensor. SPR biosensors are often

Institute of Photonics and Electronics of the Czech Academy of Sciences, Chaberská 1014/57, 182 51 Prague, Czech Republic. E-mail: homola@ufe.cz; Fax: +420 284 681 534; Tel: +420 266 773 404

† Electronic supplementary information (ESI) available: The ESI includes details related to the prediction of mass transfer coefficients (and selected fitted sensorgrams) for all three substrate configurations and flow cells. See DOI: 10.1039/c9lc00699k

‡ Present address: Department of Physics, Chalmers University of Technology, 412 96 Göteborg, Sweden.

§ Present address: Center for Nanotechnology Innovation, Istituto Italiano di Tecnologia, 561 27 Pisa, Italy.

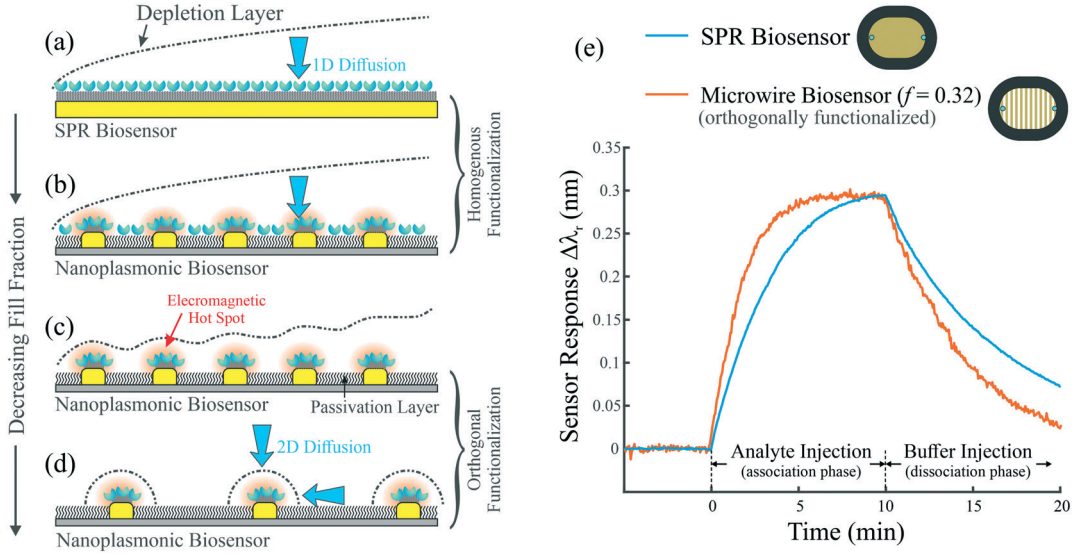

Fig. 1 The shape of the analyte depletion layer (dotted-dashed lines), and thus the rate of analyte transport, is dependent on the nanoplasmonic architecture. (a) A SPR biosensor will have similar analyte transport characteristics as (b) a uniformly functionalized nanoplasmonic biosensor, both having depletion layers of similar size. (c) When orthogonally functionalized, the same nanoplasmonic biosensor will exhibit a thinner analyte depletion layer (more complex in shape), along with increased rates of transport. (d) When the fill fraction of a nanoplasmonic biosensor is sufficiently low, the depletion layer will be hemispherical and much smaller in size than in case (a), where analyte transport, proceeding solely *via* diffusion, is two-dimensional, allowing for further increases in analyte transport. (e) Sensorgrams taken from both a SPR- and microwire-based biosensor using the same flow cell (details below, l = 10 μm, c = 10 nM); the increased sensor response for the microwire biosensor (in both the association and dissociation phases) is directly attributed to increased analyte transport.

subject to severe diffusion limitations, where a lack of fluid movement adjacent to the sensing surface results in a zone of depleted analyte (depletion layer) that grows in size along the flow direction (Fig. 1a).[15] When uniformly functionalized, a nanoplasmonic biosensor of similar size will exhibit a similar depletion layer (Fig. 1b). Conversely, analyte transport to an orthogonally functionalized nanoplasmonic biosensor will exhibit more complex depletion layers (Fig. 1c), where the passivated regions between plasmonic elements allow for depletion layer recovery and furthermore, enhanced rates of transport. When plasmonic elements become sufficiently far apart from one another, the depletion layers (with a size of the same magnitude as a single plasmonic element) become hemispherical in shape and smaller in size, leading to even higher rates of transport (Fig. 1d). Fig. 1e demonstrates how this phenomenon is manifested experimentally, where we compare the sensor response of a SPR biosensor with that of a microwire-based biosensor. The two sensors exhibit similar optical sensitivity (seen in the similar responses at equilibrium), however, the time to reach equilibrium for the microwire biosensor is much shorter: an effect solely attributed to an increase in analyte transport.

Hence, when orthogonally functionalized, the rate of analyte transport, and thus the sensor response, will be strongly influenced by the nanoplasmonic architecture – both in the size and shape of each plasmonic element as well as their spacing with respect to each other. Prediction of such transport rates to complex substrates (useful for sensor optimization) was unavailable until recently, when using the results of several numerical methods we proposed a simple analytical approach to estimate transport to array-based sensors.[16] We later demonstrated this effect experimentally, showing that the sensing performance for a nanoplasmonic biosensor is dependent on the product of optical performance with the rate of analyte transport.[17]

In this study we examine the analyte transport characteristics to a wide range of micro- and nanoplasmonic biosensors, all of which are practically relevant within the current literature. We examine the biosensing characteristics of plasmonic substrates having three configurations – based on microwires, nanorods, and nanodisks – with the former two having variable coverage of plasmonic elements. These substrates are functionalized using multiple analyte/receptor systems based on both DNA and RNA oligonucleotides. Sensorgrams created from individual channels on each substrate are used to extract both kinetic data (association and dissociation rate constants) as well as the rate of analyte transport (mass transfer coefficient). We show that, across all substrates, experimental measurements of analyte transport match very well to our previously developed analytical model.

This study serves as an experimental verification of our previously developed analytical model,[16] which had only been partially verified through experiments limited to only nanorod based substrates used for the detection of a single analyte.[17] Altogether, rather than focusing on optical characteristics, this study highlights the characteristics of analyte transport across many types of heterogeneous sensing surfaces. In addition to being relevant to the nanoplasmonic configurations shown herein (*i.e.*, sensors based on microwires, nanodisks, and nanorods), these results are

applicable to a majority of current nanoplasmonic biosensor designs used in a flow-over format. The results shown herein can be used to design optimal architectures for nanoplasmonic biosensing.

Background and methodology

Fig. 2 shows the three nanoplasmonic configurations and associated microfluidic channels considered in this study. Plasmonic substrates exhibited a unique reflectance spectra having a plasmonic feature (minimum or maximum) at a wavelength λ_r. The sensor response was calculated as the shift of this position ($\Delta\lambda_r$) as a result of changes in the surface density of captured analyte ($\Delta\Gamma$), where the proportionality between these changes defines the sensitivity $S_\Gamma = \Delta\lambda_r/\Delta\Gamma$, determined by the optical characteristics of each sensor.

We consider the microfluidic-based delivery of analyte to the sensing surface, where each microchannel has height H, width W, and the sensing region has length L. Nanoplasmonic sensors consist of individual gold plasmonic elements with characteristic length l (in the direction of flow), width w (orthogonal to flow), and height h. Each sensing substrate had a fill fraction f, defined as the ratio of the overall surface area of the plasmonic elements with respect to the projected surface area of the sensing surface (Fig. 2); by this definition, SPR-based sensors (having a continuous gold film) have a fill fraction of $f = 1$.

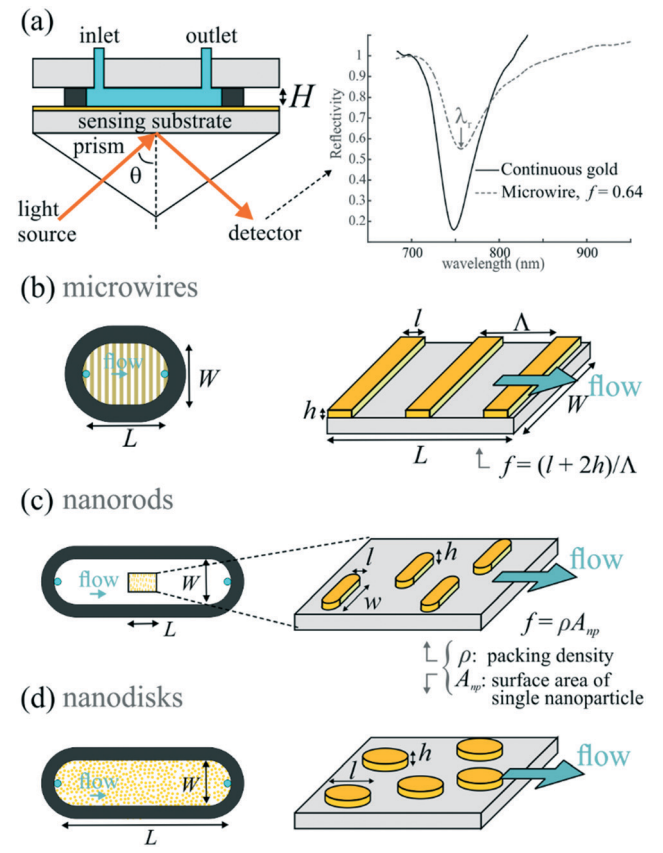

Fig. 2 (a) Schematic of the microfluidic flow cells and reflectance spectra for the substrates used in this study, specifically, configurations based on (b) microwires, (c) nanorods, and (d) nanodisks.

A liquid solution having an analyte concentration c is flowing through the sensing chamber. After transport to the sensing surface, analyte is captured in a 1:1 manner by functionalized bioreceptors having a surface density Γ_o (on each gold plasmonic element). Such capture can be described by both the association rate constant k_1 and the dissociation rate constant k_2. Using a quasi-steady approximation, time-rate changes in the sensor response can be described analytically as[18]

$$\frac{d\lambda_r}{dt} = S_\Gamma\left(\frac{k_1 c(\Gamma_o - \Gamma) - k_2\Gamma}{1 + k_1(\Gamma_o - \Gamma)/k_m}\right) \quad (1)$$

The value k_m represents the steady-state, diffusion-limited mass transfer coefficient, and is a measure of the efficiency of analyte transport; k_m is related to the analyte flux to the sensor surface J (averaged over the entire active surface) *via* $k_m = J/c$.

Analyte transport to a uniformly functionalized SPR biosensor is a relatively well studied topic. The mass transfer coefficient for a continuous gold film (here noted as k_p) situated in a rectangular geometry is dependent on the geometry of the microchannel (H, W, L), the diffusivity of the analyte D, and the volumetric flow rate Q. For flow in rectangular flow cells (with a single capture surface), k_p can be accurately predicted using a truncated solution proposed by Newman[19] as

$$k_p = 1.47\left(\frac{QD^2}{LH^2W}\right)^{\frac{1}{3}}. \quad (2)$$

Conversely, analyte transport to a nanoplasmonic biosensor is a much more complex problem. The study of transport to a heterogeneous reactive/passivated surface has only been recently examined, where several authors examined the problem theoretically from a microscopic perspective,[20,21] and we examined the problem from a macroscopic perspective.[16] In our model, the mass transfer coefficient to a nanoplasmonic sensor is predicted to follow

$$k_m = k_p\frac{R_k - f}{R_k f - 2f + 1}, \quad (3)$$

where $R_k = k_{np}/k_p$ is a ratio of the mass transfer coefficient for an individual plasmonic element composing the array (k_{np}), existing outside the influence of any other functionalized elements, with respect to the mass transfer coefficient for a continuous surface (k_p). In this study k_{np} would be representative of experiments consisting of a single microwire, nanodisk, or nanorod (we have also proposed a model to predict k_{np} to single nanodisks and nanorods[22]). From eqn (3) (when $R_k \gg 1$) it can be seen that as the fill fraction approaches unity ($f \rightarrow 1$), the mass transfer coefficient to an array approaches that to a continuous film

($k_m \rightarrow k_p$) and furthermore, scales inversely to the fill fraction ($k_m \sim k_p f^{-1}$) in the region of $f \approx 1$.

Eqn (1) is routinely used to extract kinetic parameters (k_1, k_2) from sensorgrams taken *via* the SPR method, specifically through fitting of eqn (1) to experimental data obtained at various analyte concentrations.[18] This equation also provides insight into the nature of affinity capture during a biosensing assay. The term $Da = k_1\Gamma_o/k_m$ represents the Damköhler number: a dimensionless parameter that represents the ratio between the rate of (reactive) affinity analyte capture with respect to the rate of analyte transport to the sensor surface.[15] The form of this term corresponds to the beginning of a detection experiment, where the surface density of captured analyte is very small ($\Gamma \approx 0$). Affinity capture is considered to be diffusion-limited when $Da \gg 1$, and reaction-limited when $Da \ll 1$.

When the Damköhler number is on the order of unity ($Da \approx 1$), contributions of both reactive and transport effects to the sensor signal are of similar magnitude. Therefore, in this regime one can use eqn (1) to extract both kinetic and mass transport parameters from sensorgram data. For the experiments shown herein, we thus used different analyte/receptor pairs for each substrate as to maintain $Da \approx 1$. Sensorgrams taken from each substrate, consisting of multiple injections with variable c, were used to obtain information on k_1, k_2 and k_m. This method provides an internal standard, as experiments using substrates having different fill fractions (similar configuration, analyte/receptor pairs, and detection conditions) will only lead to changes in measured mass transport behavior (k_m), where measurements of kinetic behavior are not expected to change (k_1, k_2).

The results herein are applicable to sensors operated in a flow over format, which are representative of the vast majority of previous work on nanoplasmonic biosensors. These results cannot be directly applied to flow through nanoplasmonic biosensors, which in a limited number of works, have been shown to overcome diffusion limitations (*via* flow directly adjacent to, and through, the sensing surface).[23–25] In a similar fashion, these results do not apply to sensors where analyte transport occurs through active means (*e.g.*, (di)electrophoresis).

Results

Plasmonic elements on each sensing substrate were functionalized with thiol-derivatized DNA or RNA sequences that were complementary to a target analyte, whereas the glass surfaces were untreated. We assumed no interaction between analyte and the glass surface, as both the analyte (ssDNA/ssRNA) and glass surface have a slight negative charge under the conditions of the assay.[26] The fill fraction was calculated for each substrate according to the equations shown in Fig. 2. For all flow cells and analyte/receptor pairs we also performed experiments using a continuous gold layer (*i.e.*, SPR biosensor, $f = 1$).

There were 2–5 individual measurement channels on each sensing substrate, from which we recorded the sensor response during the injection of analyte (association phase), followed by an injection of buffer without analyte (dissociation phase). The sensor surface was regenerated after each cycle. Sensorgrams taken from individual channels consisting of 3–6 injections (association and/or dissociation phases measured with variable analyte concentration) were used to extract characteristic interaction parameters, specifically k_1, k_2, Γ_o, and k_m (or k_p for SPR-based measurements). Unless noted, all experiments were conducted under conditions such that $0.1 < Da < 12$.

For both the continuous gold surfaces and large microwire substrates we assumed a sensitivity of $S_{\Gamma,SPR} = 5.56$ nm mm^2 ng^{-1}, which corresponds to the sensitivity of a propagating surface plasmon with a resonant wavelength of 750 nm to the addition of a 5 nm thick dielectric adlayer (RI = 1.43).[17] This value was used to estimate the probe density (Γ_o) for each analyte/receptor pair in each flow cell (*via* data taken from continuous gold films). The sensitivities of other substrates were estimated *via* the ratio between the average fitted value of Γ_o between a micro- or nano-structured substrate and that for a continuous gold surface, multiplied by $S_{\Gamma,SPR}$. The data shown in Fig. S1, S3, and S5 (ESI†) give representative values of the sensitivities across all of the substrates and fill fractions that we utilized in experiment.

Microwire experiments

We fabricated 21 substrates based on microwires of both varying wire size ($l = 1.4$, 10, 100 μm) and fill fraction ($0.16 < f < 0.64$), where each substrate had 2 measurement channels and 2 reference channels. The microwires were aligned with their long axis parallel with the plane of incidence (TM polarization). We performed experiments using two different target DNA oligomers complementary to a single probe sequence (Fig. 3a). Example sensorgrams for both a microwire substrate and a continuous gold surface are shown in Fig. 3d and e.

The normalized reflectance spectra taken from substrates based on larger microwires ($l = 10$, 100 μm, Fig. 3b) exhibited spectral dips which correspond to the excitation of propagating surface plasmons, where the contrast of the spectral dips decreased with decreasing fill fraction. We observed no significant difference in the high concentration equilibrium sensor response between the larger microwire substrates ($\Delta\lambda_r = 0.47 \pm 0.08$ nm, 26 sensorgrams) and continuous gold films ($\Delta\lambda_{r,SPR} = 0.45 \pm 0.08$ nm, 4 sensorgrams). This similarity suggests that the larger microwire substrates have a sensitivity equivalent to the continuous gold surface, which is consistent with the work by Sarkar *et al.*[9] concerning wires with dimension $l \gg \lambda_r$. These data lead to a density of immobilized probes of $\Gamma_o = 2.6 \pm 0.5 \times 10^{-14}$ mol mm^{-2}.

Conversely, the normalized reflectance spectra taken from the smaller microwire substrates ($l = 1.4$ μm, Fig. 3c) show a

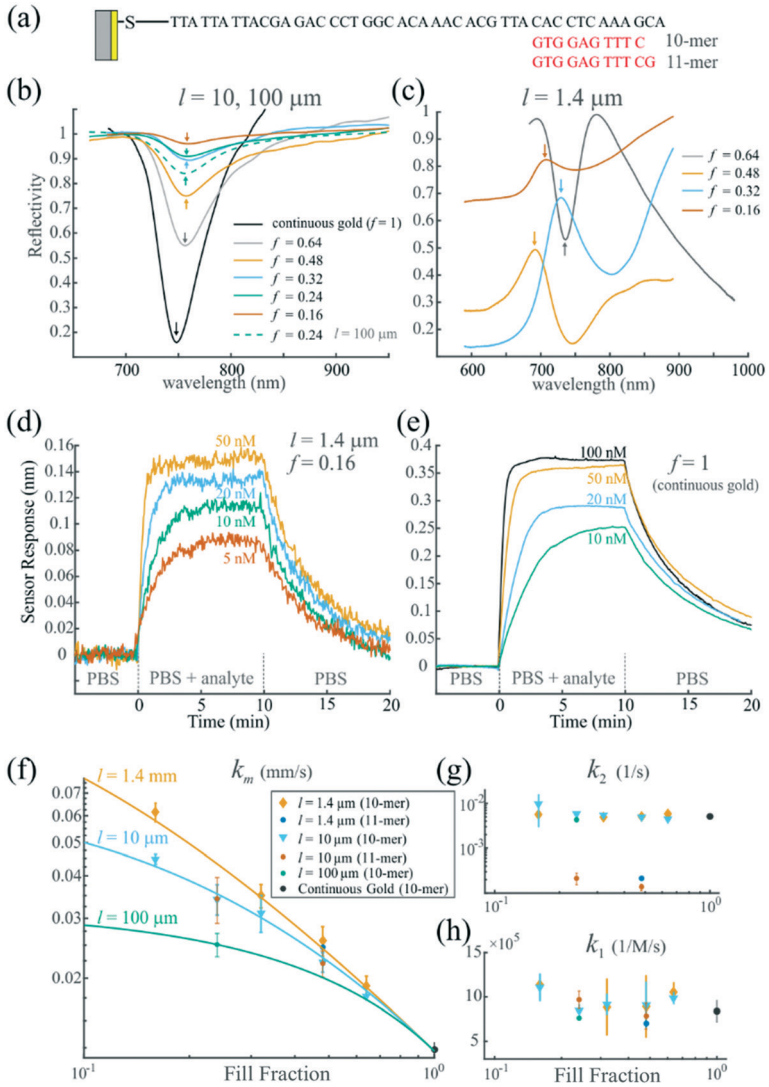

Fig. 3 Microwire experiments. (a) Schematic for the DNA receptor/analyte system. Reflectivity spectra for microwire sensing substrates for (b) larger (l = 10, 100 μm) and (c) smaller (l = 1.4 μm) microwires at varying fill fraction. Arrows indicate the plasmonic feature tracked during experiment. Selected sensorgrams (10-mer analyte) for both (d) a microwire substrate (f = 0.16, l = 1.4 μm) and (e) a continuous gold surface; fitted sensorgrams are shown in Fig. S1.† (f) Extracted values of k_m across all microwire substrates. Symbols represent experimental data; solid lines represent the predicted response for each microwire size (*via* eqn (3)). Extracted values of both (g) k_2 and (h) k_1 across all microwire substrates.

more complex spectra, a result of the coupling of propagating surface plasmons with lattice resonances.[27] These sensors were observed to exhibit a lower sensitivity, where the high concentration equilibrium sensor responses for smaller microwires were lower than that for a continuous gold surface (Fig. 3d and S1†).

Extracted values of k_m, k_2, and k_1 across all microwire substrates for both analytes are shown in Fig. 3f–h. A selection of fitted sensorgrams along with their extracted parameters are shown in Fig. S1.† It can be seen that extracted association rate constants are similar for both target sequences; however, dissociation rate constants for the 11-mer sequence are lower by over an order of magnitude with respect to those for the 10-mer sequence. We observed a large increase in the mass transfer coefficient with decreasing fill fraction, with larger increases observed for microwires having smaller dimension. No differences were seen in k_m between experiments using the two target analytes for a given substrate. Predictions for k_m as a function of the fill fraction match well with experimental data (Fig. 3f); the ESI† gives details on these predictions, along with information on both experimental and predicted parameters (Table S1).

Nanodisk experiments

We fabricated a single substrate with nanodisks arranged in a random packing order covering the entire floor of the sensing microchannel. The RNA analyte/receptor scheme is shown in Fig. 4a. In hybridized form this pair exhibits a stem-loop structure with an adenine bulge,[28] but otherwise demonstrated typical 1 : 1 binding kinetics. Fig. 4b shows the

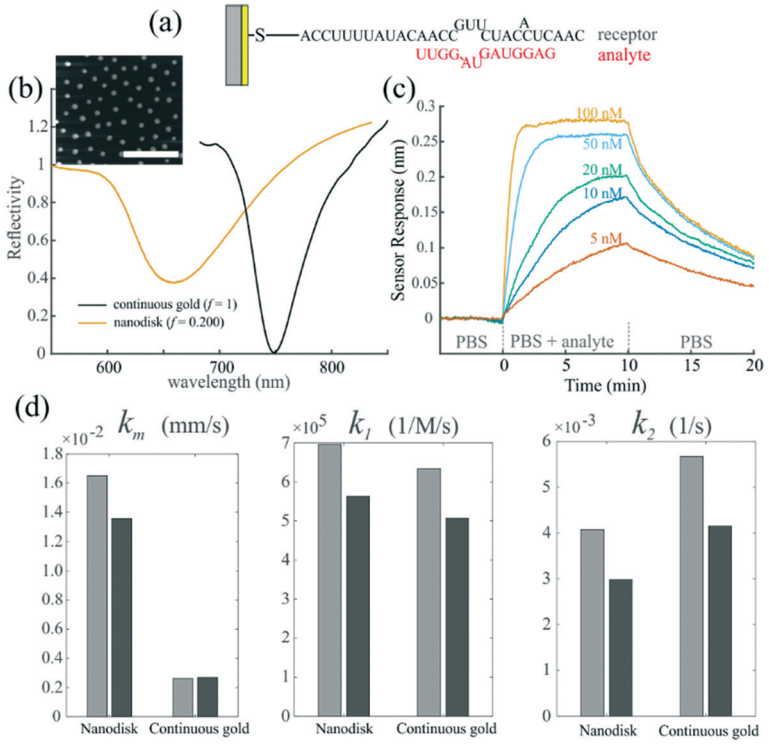

Fig. 4 Nanodisk experiments. (a) Schematic for the RNA receptor/analyte system. (b) Normalized reflectivity spectra for both a nanodisk substrate and a continuous gold film. The inset shows a SEM image of the nanodisk sensing substrate (scale bar 1 μm), where the disks had a mean diameter of l = 88 ± 8 nm. (c) Representative sensorgram for the nanodisk substrate. (d) Extracted values of k_m, k_1, and k_2 for both nanodisk and continuous gold substrates (using the same flow cell). Each bar represents data taken from a single sensorgram.

reflectance spectra of the substrate, where the dips in the reflectance spectra correspond to the excitation of longitudinal localized surface plasmons (TE polarization). From a SEM image we calculated a mean diameter of l = 88 ± 8 nm (h = 30 nm) and packing density of ρ = 13.9 μm^{-2}. The fill fraction was thus estimated as $f = \rho A_{np} = 0.200$.

We obtained two sensorgrams from both the nanodisk substrate (a single sensorgram is shown in Fig. 4c) and a continuous gold surface. The high concentration equilibrium sensor response for the continuous gold film ($\Delta\lambda_{r,SPR}$ = 1.42 ± 0.07 nm) led to a density of immobilized probes of Γ_o = 6.2 ± 0.3 × 10^{-14} mol mm^{-2}; data for the nanodisk substrates was lower ($\Delta\lambda_r$ = 0.281 ± 0.005 nm), indicating these substrates had a lower sensitivity; these values, along with fitted sensorgrams and other associated data, are shown in Fig. S3.†

Extracted values of k_m, k_2, and k_1 taken from nanodisk substrates are shown in Fig. 4d. We observed little difference between extracted values of k_1 and k_2 taken from nanodisk and continuous gold experiments, and a large difference in extracted values of k_m. Predicted values for the mass transfer coefficient for the nanodisk array (k_m = 0.0258 mm s^{-1}) and continuous gold film (k_m = 0.0052 mm s^{-1}) differed from average experimental values by a factor of 1.72 and 1.92, respectively (Table S2†). The differences between prediction and experiment are likely attributed to both the more complex flow cell design and the presence of nanodisks across the entire floor of the sensing chamber (outside of the interrogated region, Fig. S4†).

Nanorod experiments

We fabricated 6 substrates with nanorods arranged in a random packing order, having their long axis arranged parallel with the polarization of incident light (TE polarization). Substrates were fabricated with varying fill fraction, determined as $f = \rho A_{np}$, where A_{np} was calculated as the surface area of a rectangular block (l = 30 nm, w = 110 nm, h = 30 nm). An SEM image of one substrate can be seen in Fig. 5b, and details on the flow cell are shown in Fig. S6.† The dips in the reflectance spectra (Fig. 5b) correspond to the excitation of longitudinal localized surface plasmons. An example sensorgram taken from a nanorod substrate is shown in Fig. 5c (association phase only); we tested two chips per fill fraction, where each chip had 3 measurement channels. We observed a slight difference between the equilibrium response (high concentration) observed using a continuous gold film ($\Delta\lambda_{r,SPR}$ = 1.01 ± 0.12 nm, 6 sensorgrams, leading to Γ_o = 2.89 ± 0.34 × 10^{-14} mol mm^{-2}) and that using the nanorod substrates ($\Delta\lambda_r$ = 1.24 ± 0.21 nm, 18 sensorgrams), with no significant differences across different nanorod fill fractions, which we also observed in our previous study.[17]

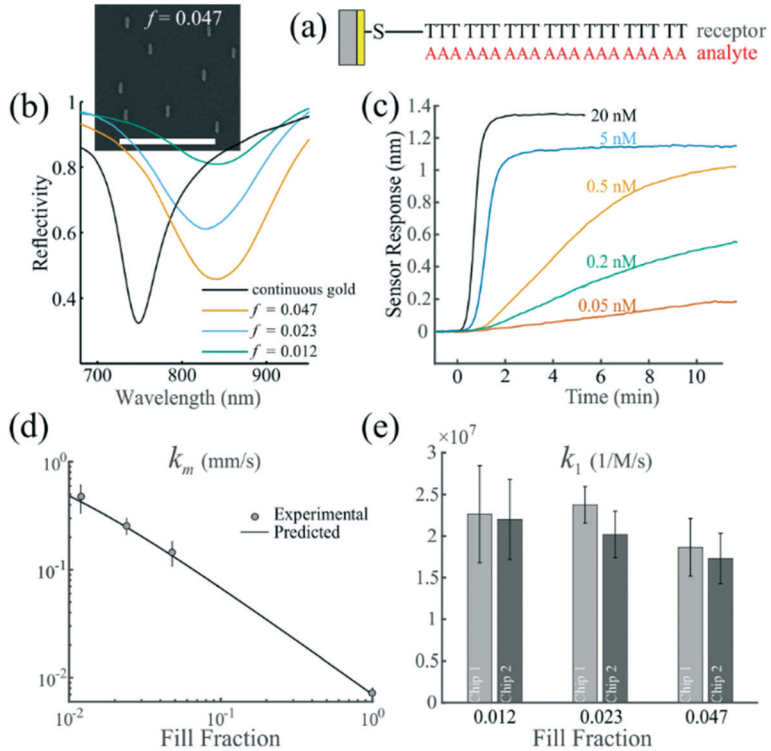

Fig. 5 Nanorod experiments. (a) Schematic for the DNA receptor/analyte system. (b) Reflectivity spectra for the nanorod substrates along with the continuous gold surface. (inset) SEM images of a nanorod substrate (scale bar 1 μm); individual nanorods had dimensions of l = 30 nm, w = 110 nm, and h = 30 nm. (c) Sensorgram for a nanorod substrate (f = 0.023). (d) Extracted values of k_m across all substrates. The solid line represents the predicted response. (e) Extracted values of k_1 for the nanorod substrates (3 sensorgrams per chip).

Extracted values of k_m for the nanorod substrates are plotted as a function of the fill fraction in Fig. 5d; experimental data match well with analytical predictions (Table S3†). There was little difference in the extracted values of k_1 across all nanorod substrates (Fig. 5e). Due to severe diffusion limitations (Da > 50), we did not obtain data for k_1 from continuous gold experiments; however, in that regime, extracted measurements of k_p can be considered to be accurate. The good match between predicted and experimental values of k_p and k_m suggests that there was little to no interaction between the ssDNA analytes and the non-functionalized glass surfaces.

Discussion

The experimental design used herein, *i.e.*, the use of different analyte/receptors for each substrate (each having a different association rate constant), ensured that all measurements were taken in the range of Da ≈ 1. These conditions allowed us to extract both kinetic and mass transfer parameters from sensorgrams using methods that are commonly used in biomolecular interaction analysis. When considering a single analyte/receptor system, the kinetic data (k_1, k_2) collected in this study show little dependence on the fill fraction across each substrate configuration, whereas as expected, extracted values of k_m vary significantly with changes in the fill fraction. Therefore, it is likely that the extracted values of k_m are void of artifact. The strong match between observed and predicted values of k_m across all substrates also suggests that other transport effects (*e.g.*, thermophoresis) are very limited under the conditions used here.

To directly compare the analyte transport behavior across the three experimental substrate configurations (and three different flow cells), we calculated the mass transfer enhancement $E = k_m/k_p$ for all of the experimental data shown above. These data are plotted in Fig. 6. In addition, using existing analytical solutions for analyte transport, we predicted R_k (*via* predictions of k_{np} and k_p) for all of the substrate configurations used herein; these predictions are detailed in the ESI† (Tables S1–S3). From the data shown in Fig. 6, it can be seen that the values predicted by eqn (3) match well to all of the experimental data taken across all fill fractions.

Design guidelines

The results shown herein have fairly strong implications for the design of a nanoplasmonic sensor: the rate of mass transport to a nanoplasmonic structure is strongly dependent on both the sensor fill fraction as well as the specific plasmonic architecture (where the difference in size between individual plasmonic elements and the overall sensing region will determine R_k). Thus, two different plasmonic nanostructures having similar R_k and f will have similar mass

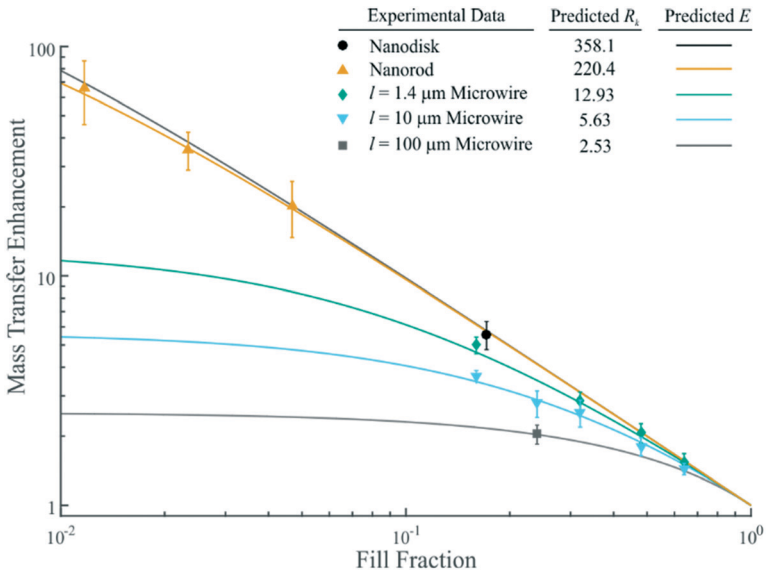

Fig. 6 Mass transfer enhancement ($E = k_m/k_p$) plotted *vs.* the fill fraction for all of the experimental substrates (symbols). All experimental data scale according to eqn (3), data from which are shown as the solid lines using respective values of R_k for each substrate.

transport characteristics, regardless of the substrate configuration or packing order. The value R_k is strongly dependent on the size and shape of an individual plasmonic element. Plasmonic structures having individual elements with smaller characteristic sizes will have higher R_k (and have a stronger dependence on the fill fraction), seen explicitly in the data herein taken from microwire substrates. A same argument holds related to how much an individual plasmonic element protrudes into the sensing medium: positive relief elements will have higher R_k with respect to negative relief elements (*e.g.*, nanohole) having similar characteristic sizes. Eqn (3) also sets the upper limit for mass transport, where the mass transfer enhancement for any nanostructure cannot exceed $E = 1/f$ (seen from eqn (3) as $R_k \rightarrow \infty$).

These results also suggest interesting behavior for plasmonic sensors based on *N*-particle clusters, for which an individual plasmonic element is represented by an individual cluster composing the array (larger size, smaller R_k), and not a single element (smaller size, larger R_k). Thus, at equal fill fraction, analyte transport to an array of clustered plasmonic elements (*e.g.*, nanodisk heptamers) is expected to be lower than that to an array of non-clustered elements. The difference in transport rates to *N*-particle clusters (*vs.* that to a non-clustered array) will increase as the overall size of the cluster increases.

For nanostructures with fill fraction such that $f > 1$, such as an array of high aspect ratio nanoparticles, mass transport should continue to scale as $E = 1/f$, with lower rates of transport compared to a continuous gold surface. As follows, nanoplasmonic structures that are not functionalized in a orthogonal manner (having immobilized receptors along the entire sensing surface) will have a fill fraction of $f \geq 1$, and will exhibit mass transport properties that are equal to (or less than) a sensor based on a continuous gold film. This property highlights the importance of the use of orthogonal functionalization methods for nanoplasmonic biosensors.

Conclusions

In summary, we have investigated the analyte transport characteristics for a wide range of micro- and nanoplasmonic substrates, with variations of both the substrate configuration (individual elements based on microwires, nanodisks, and nanorods) as well as the substrate fill fraction. Rates of analyte transport, quantified here as the mass transport coefficient, were obtained *via* the kinetic analysis of sensorgrams taken from individual channels on each substrate. We utilized multiple analyte/receptor pairs within (and across) different substrate configurations to ensure accurate measurements of both kinetic and mass transport data. In addition to their dissimilar sensing architectures, the substrates tested herein have vastly different spectral profiles and sensitivities. However, we show that the analyte transport characteristics across all substrates follow similar characteristics, which are dependent both on the sensor fill fraction f as well as the nature of the individual plasmonic elements composing the substrate (defining R_k), and invariant to the substrate configuration or packing order (random or periodic). Rates of transport across all substrates match well to those predicted by eqn (3), proposed in a previous study,[16] of which the results herein serve as an experimental verification.

The results of this study confirm that analyte transport to nanoplasmonic biosensors can be accurately predicted using a simple analytical model. This model, given by eqn (3) in the form of a mass transfer coefficient (k_m), can be applied to nearly all affinity-based nanoplasmonic biosensors in the

current literature. Along with knowledge of the kinetic parameters related to an affinity-interaction, these predictions can be used to predict the rate of analyte capture across both diffusion- and reaction-limited conditions (*via* eqn (1)). In terms of design optimization, these predictions are especially valuable when used with other methods to predict the optical characteristics of these sensors.

Material and methods

Fabrication of sensing substrates

All plasmonic substrates consisted of gold structures on a glass chip, fabricated *via* lift-off.

Microwire. Microwire lift-off templates were fabricated *via* UV lithography, where clean glass substrates were spin-coated (Laurell WS650, 4500 rpm, 60 s) with Microposit S1805 (Dow Chemical) and soft baked on a hot plate (120 °C, 120 s). Patterns corresponding to a microwire array (6 × 11 mm^2 overall size) were written by direct write laser lithography (MicroWriter ML2, Durham Magneto Optics) using a 1 μm, 405 nm laser. The samples were then post baked on a hot plate (120 °C, 120 s) and developed (75 s, Microposit MF-319, Dow Chemical) using mild agitation.

Nanodisk. Nanodisk lift-off templates were fabricated *via* hole-mask colloidal lithography, where clean glass substrates were spin-coated (3000 rpm, 60 s) with poly-(methylmethacrylate) (PMMA, 2% solution in anisole, 950 kDa, MicroChem) and soft baked on a hot plate (120 °C, 10 min). This layer was immersed into a 0.2% solution of polydiallyldimethyl ammonium (PDDA) for 30 s, rinsed with Milli-Q water (Q-water), and gently dried with nitrogen. The substrate was then immersed in a solution of sulphonated polystyrene particles (PPs, 110 nm mean diameter, 0.2% weight, Life Technologies, Czech Republic) for a short period, rinsed with Q-water, and gently dried with nitrogen, after which a 25 nm thick gold film was deposited *via* e-beam evaporation (UHV 350, Balzers). The PPs were removed *via* stripping with tape, after which the PMMA on the bottom of each nanohole was removed with oxygen plasma (10 min).

Nanorod. Nanorod lift-off templates were fabricated *via* e-beam lithography, where clean glass substrates were subsequently spin-coated (Laurell WS650, 3000 rpm, 30 s) with two layers of PMMA having different molecular weights (495 and 950 kDa, 2% solution in anisole, MicroChem Corp.), and soft-baked on a hot plate (120 °C, 120 s), after which a conductive polymer layer (AquaSAVE, Mitsubishi Rayon) was spin-coated (2500 rpm) and soft-baked (100 °C, 120 s). Patterns corresponding to a nanorod array (randomly distributed, overall size of 2 × 1 mm^2 for each sensing channel) were exposed *via* an electron beam (Raith eLINE Plus, 20 kV), after which the AquaSAVE layer was washed off by purified water. Samples were developed for 30 s in a 3 : 1 mixture of isopropyl alcohol (IPA) : methyl isobutyl ketone (MIBK), followed by immersion in IPA for 30 s.

Metal layers were deposited on all substrates using e-beam evaporation (microwires: 1.5 nm Ti, 50 nm Au; nanodisks: 1.5 nm Ti, 30 nm Au; nanorods: 1.5 nm Cr, 30 nm Au). Lift-off was carried out *via* sonication (Elmasonic P30H) in either acetone (nanorod, nanodisk substrates) or Mr-Rem700 (microwire substrates, Dow Chemical). Sensing substrates consisting of a continuous gold film (1.5 nm Ti, 50 nm Au) were produced by evaporation of metal layers onto either the entire glass substrate (microwires, nanodisks) or onto an array of 2 × 1 mm^2 rectangles (nanorods).

Optical and microfluidic setup

We used a multi-channel laboratory SPR platform with wavelength interrogation developed at the Institute of Photonics and Electronics (Prague). Optically, the sensor is based on the Kretschmann geometry using the attenuated total reflection method, where light from a halogen lamp (Ocean Optics, HL-2000-HP-B) is sent through a collimator, dichroic polarizer, and an optical prism (BK7 glass) interfaced to the sensing substrate *via* an index matching fluid. Reflected light was collected by a custom-built spectrograph (based on a gold diffraction grating) using a CMOS camera (Basler, acA1920-155um). Normalized reflectivity spectra were obtained *via* the ratio of the dark-noise corrected reflectance intensity with either (a) the dark-noise corrected reflectance from a plain glass slide (nanorods, nanodisks), or (b) the dark-noise corrected reflectance from a sensing substrate exposed to air (microwires). The sensor output (λ_r) was taken as the position of either the reflectance dip (nanodisks, nanorods, l = 10, 100 μm microwires) or the reflectance maximum (l = 1.4 μm microwires), where λ_r corresponded to the geometrical center of the spectral feature having intensities lower than 40% of its depth. Fluidic channels are formed by sealing a series of four open faced microchannels of similar design (consisting of vinyl gaskets glued to an acrylic flow cell with machined input/output ports) to a sensing substrate. The vinyl gaskets had a thickness of H = 50 μm, where the horizontal microchannel design was slightly different across experiments (shown in detail in Fig. S2, S4 and S6†). A multichannel peristaltic pump (Ismatec, ISM931C) was used to deliver samples to each channel on the flow cell, which for microwire and nanodisk experiments used passive fluidic switching described previously (with further descriptions of the flow cells used herein).[29] The flow cell and sensing substrate were maintained at a temperature of 25 °C during all experiments.

Biosensing experiments

All biosensing experiments were conducted in a similar fashion, with only slight changes in reagents and functionalization protocols between each substrate configuration.

Reagents. We used buffers of PBS (10 mM phosphate, 2.9 mM KCL, 137 mM NaCl, pH 7.4), PBS_{NaCl} (PBS + 500 mM NaCl, pH 7.4), and $Tris_{Mg}$ (10 mM Tris-HCl, 30 mM $MgCl_2$, pH 7.4). Mercaptohexanol ($HS–(CH_2)_6–OH$) was purchased

from Sigma-Aldrich. A thiolated carboxy-terminated polyethylene glycol (ctPEG, HS–$(CH_2)_{11}$–$(EG)_6$–OCH_2–COOH) was purchased from Prochimia (Poland). The DNA and RNA oligonucleotides DNA probes PR_{wire} (DNA, 5′-5ThioMC6D-iSp18-TTA TTA TTA CGA GAC CCT GGC ACA AAC ACG TTA CAC CTC AAA GCA-3′), PR_{disk} (RNA, 5′-5ThioMC6D-iSp18-ACC UUU UAU ACA ACC GUU CUA CAC UCA AC-3′), PR_{ref} (DNA, 5′-5ThioMC6D-TTA TTA TTA TTA TGC TTT GAG GTG-3′), PR_{rod} (DNA, 5′-HS-T_{20}-3′), and the oligonucleotide targets TAR_{wire1} (DNA, 3′-GTG GAG TTT C-5′), TAR_{wire2} (DNA, 3′-GTG GAG TTT CG-5′), TAR_{disk} (RNA, 5′-5Phos-GAG GUA GUA GGU U-3′), and TAR_{rod} (DNA, 5′-A_{20}-3′) were purchased from Integrated DNA Technologies (USA). All other chemicals were of analytical grade.

Microwire and nanodisk functionalization. Before functionalization, substrates were rinsed with ethanol and Q-water, cleaned with ozone for 10 min, rinsed with ethanol and Q-water, and dried with nitrogen. Substrates were then mounted into the SPR setup. A short injection of PBS buffer (<5 min) was then followed by a 25 minute injection of 200 nM probes in PBS (measurement channels for microwire and nanodisk substrates had PR_{wire} and PR_{disk}, respectively, and reference channels for both had PR_{ref}), followed by a 5 minute injection of PBS, a 15 minute injection of ctPEG (microwires) or mercaptanol (nanodisks), a 3 minute injection of PBS_{NaCl}, and finally a sustained injection of PBS (running buffer).

Nanorod functionalization. Before functionalization, substrates were rinsed with ethanol and Q-water, dried with nitrogen, and immersed in a solution of 4 : 3 : 28 NH_3 : H_2O_2 : Q-water for 30 minutes (40 °C). Substrates were then rinsed with Q-water, dried with nitrogen, and cleaned with ozone for 10 min. Substrates were then immersed overnight in a refrigerated solution of probes (2 μM PR_{rod}) in $Tris_{Mg}$. Substrates were then rinsed with Q-water, dried with nitrogen, mounted to the SPR prism using an index matching fluid, and sealed to a flow cell. An injection of mercaptohexanol (1 M, 20 min) was followed by a 5 minute injection of PBS, a 5 minute injection of 2 mM NaOH, a 5 minute injection of PBS, and a sustained injection of $Tris_{Mg}$ (running buffer).

Experimental protocol. Before analyte injection, running buffer was pumped for a minimum of 10 minutes to obtain a stable baseline, after which target analytes at variable concentration (microwires: TAR_{wire1} and TAR_{wire2}; nanodisks: TAR_{disk}, nanorods: TAR_{rod}) were injected for a period of 10–15 minutes (association phase), followed by an injection of running buffer for at least 20 minutes (dissociation phase). After each association/dissociation cycle, substrates were regenerated with 5 mM NaOH for 2 minutes. Sensor responses were corrected for long term drift, and for microwire and nanodisk experiments, the reference channel response was subtracted from the measurement channel. All injections for each sensorgram were obtained from the same detection channel. Aside from variable flow cells and receptor/analyte pairs, other assay conditions (flow rate, microchannel height, and temperature) were constant across all experiments.

Analysis of sensorgrams

All sensorgrams were analyzed to extract bioanalytical information as follows. We assumed that analyte was captured in a 1 : 1 manner by immobilized bioreceptors, which has been successfully used in a number of studies relevant to the kinetic analysis of solid phase DNA hybridization.[30–32] Under such capture mechanism, when mass transport effects are included (*i.e.*, using a two compartment model), the time-rate sensor response can be described according to eqn (1).[18]

We used non-linear least squares optimization to extract the parameters k_1, k_2, Γ_o, and k_m from experimental sensorgrams (3–6 injections at variable c) taken from individual channels. Specifically, after providing initial estimates of $k_1 = 1 \times 10^6$ 1/M s^{-1}, $k_2 = 4 \times 10^{-4}$ 1/s, $S_\Gamma\Gamma_o = 0.45$ nm, and $k_m = 0.035$ mm s^{-1}, we searched for a minimum in the vector difference between the time-series experimental data and the solution to eqn (1). At each iteration the solution to eqn (1) was obtained *via* ode23 with relative and absolute tolerances of 10^{-6}, Jacobian values were calculated using finite differences, and the best-fit values of k_1, k_2, Γ_o, and k_m were updated. Iterations were terminated when the squared 2-norm of the residual was below 10^{-6} (<2000 iterations). The nanorod experiments did not use passive fluidic valving, thus for those sensorgrams we modified c as a function of time to account for axial dispersion *via* the results of Taylor.[33]

For each fit we allowed k_1, k_2, and k_m to be global parameters. The probe density Γ_o was set to be a local parameter for each injection, as there was a small deviation in the probe density for each injection due to the sequential nature of obtaining each sensorgram from a single channel (incomplete regeneration after each injection cycle). We observed only a small deviation in fitted values of Γ_o across all injections for each channel on each substrate (Fig. S1, S3 and S5†). In addition, we observed only a small difference in extracted values of k_1, k_2, Γ_o, and k_m when allowing Γ_o to be a global parameter across all injections for each sensorgram. Extracted parameters had little sensitivity to initial estimates, which is highlighted in Fig. S7,† where changes in the initial estimates for k_m by over 3 orders of magnitude had little to no influence on the resulting fits for k_1, k_2, Γ_o, and k_m. Similar results were obtained *via* variation of initial estimates of k_1, k_2, and Γ_o. Results from a selected set of sensorgrams matched well with results obtained *via* commercial software (BIAevaluation 4.1).

Author contributions

N. S. L., J. S., B. Š., and J. H. conceived the concept of the study. N. S. L, J. S., B. Š., and T. Š. designed the experiments. M. G., M. L. E., B. Š., and T. Š. performed the experiments. N.

S. L. analyzed the results and wrote the manuscript. J. S., B. Š., and J. H. edited the manuscript.

Conflicts of interest

There are no conflicts of interest.

Acknowledgements

The authors wish to acknowledge Petra Lebrušková for fabrication of the nanodisk substrates, and Jan Bukáček for fabrication of the smaller microwire substrates used herein. This work was supported by the Czech Science Foundation (contract #P205/12/G118, #19-02739S), and the European Union's Horizon 2020 research and innovation program (project ULTRAPLACAD, contract #633937).

References

1 A. B. Dahlin, N. J. Wittenberg, F. Höök and S.-H. Oh, *Nanophotonics*, 2013, **2**, 83–101.
2 A. R. Ferhan, J. A. Jackman, J. H. Park, N.-J. Cho and D.-H. Kim, *Adv. Drug Delivery Rev.*, 2018, **125**, 48–77.
3 G. A. Lopez, M.-C. Estevez, M. Soler and L. M. Lechuga, *Nanophotonics*, 2017, **6**, 123.
4 B. Špačková, P. Wrobel, M. Bocková and J. Homola, *Proc. IEEE*, 2016, **104**, 2380–2408.
5 J. Homola, *Chem. Rev.*, 2008, **108**, 462–493.
6 S.-W. Lee, K.-S. Lee, J. Ahn, J.-J. Lee, M.-G. Kim and Y.-B. Shin, *ACS Nano*, 2011, **5**, 897–904.
7 J. Cao, T. Sun and K. T. Grattan, *Sens. Actuators, B*, 2014, **195**, 332–351.
8 G. K. Joshi, S. Deitz-McElyea, M. Johnson, S. Mali, M. Korc and R. Sardar, *Nano Lett.*, 2014, **14**, 6955–6963.
9 M. Sarkar, M. Chamtouri, J. Moreau, M. Besbes and M. Canva, *Sens. Actuators, B*, 2014, **191**, 115–121.
10 A. B. Dahlin, *Analyst*, 2015, **140**, 4748–4759.
11 A. M. Funston, C. Novo, T. J. Davis and P. Mulvaney, *Nano Lett.*, 2009, **9**, 1651–1658.
12 A. Hajebifard and P. Berini, *Opt. Express*, 2017, **25**, 18566–18580.
13 L. Feuz, M. P. Jonsson and F. Höök, *Nano Lett.*, 2012, **12**, 873–879.
14 L. Feuz, P. Jonsson, M. P. Jonsson and F. Hook, *ACS Nano*, 2010, **4**, 2167–2177.
15 T. M. Squires, R. J. Messinger and S. R. Manalis, *Nat. Biotechnol.*, 2008, **26**, 417.
16 N. S. Lynn Jr and J. Homola, *Anal. Chem.*, 2016, **88**, 12145–12151.
17 B. Špačková, N. S. Lynn Jr, J. Slabý, H. Šípová and J. Homola, *ACS Photonics*, 2018, **5**, 1019–1025.
18 D. G. Myszka, X. He, M. Dembo, T. A. Morton and B. Goldstein, *Biophys. J.*, 1998, **75**, 583–594.
19 J. Newman, *Electroanal. Chem.*, 1973, **6**, 279–297.
20 A. S. Sangani, *J. Fluid Mech.*, 2017, **830**, 350–368.
21 P. N. Shah and E. S. Shaqfeh, *J. Fluid Mech.*, 2015, **782**, 260–299.
22 N. S. Lynn Jr and J. Homola, *Chem. – Eur. J.*, 2018, **24**, 12031–12036.
23 F. Eftekhari, C. Escobedo, J. Ferreira, X. Duan, E. M. Girotto, A. G. Brolo, R. Gordon and D. Sinton, *Anal. Chem.*, 2009, **81**, 4308–4311.
24 S. Kumar, S. Cherukulappurath, T. W. Johnson and S.-H. Oh, *Chem. Mater.*, 2014, **26**, 6523–6530.
25 A. A. Yanik, M. Huang, A. Artar, T.-Y. Chang and H. Altug, *Appl. Phys. Lett.*, 2010, **96**, 021101.
26 S. P. Han, S. Yoda, K. J. Kwak, K. Suga and M. Fujihira, *Ultramicroscopy*, 2005, **105**, 148–154.
27 F. G. De Abajo, *Rev. Mod. Phys.*, 2007, **79**, 1267.
28 M. Cevec, C. Thibaudeau and J. Plavec, *Nucleic Acids Res.*, 2010, **38**, 7814–7821.
29 T. Špringer, M. Piliarik and J. Homola, *Sens. Actuators, B*, 2010, **145**, 588–591.
30 H. Šípová and J. Homola, *Anal. Chim. Acta*, 2013, **773**, 9–23.
31 K. Tawa and W. Knoll, *Nucleic Acids Res.*, 2004, **32**, 2372–2377.
32 F. Yu, D. Yao and W. Knoll, *Nucleic Acids Res.*, 2004, **32**, e75.
33 G. I. Taylor, *Proc. R. Soc. London, Ser. A*, 1953, **219**, 186–203.